# Time-Dependent Oxidation and Scale Evolution of a Wrought Co/Ni-based Superalloy

Cameron Crabb\*a, Zachary T. Kloennea, Samuel R. Rogersa, Chi Hang D. Kwoka, Mark C. Hardyb, Michele S. Conroy<sup>a</sup>, David Dye\*a

<sup>a</sup>Department of Materials, Royal School of Mines, Imperial College London, Prince Consort Road, London, SW7 2BP, UK <sup>b</sup>Rolls-Royce plc., Elton Road, Derby, DE24 8BJ, UK

Abstract
Understanding how protective oxide scales evolve over time is necessary for improving the long term resistance of superalloys. This work investigates the time-dependent oxidation behavior of an ingot-processable Co/Ni-based superalloy oxidized in air at 800 °C for 20h, 100h and 100oh. Mass-gain and white-light interferometry measurements quantified oxidation kinetics, surface roughness, and spallation, while high-resolution STEM-EDX characterized oxide morphology and nanoscale elemental partitioning. Atom probe tomography captured the key transition regimes between the chromia and alumina-rich scale. The oxidation rate evolved from near-linear to parabolic to a compact, dual phase chromia and alumina-rich scale. The oxidation rate evolved from near-linear to parabolic observations help link kinetics, structure and chemistry, showing how an originally porous spinel layer transforms into a dense, adherent chromia – alumina scale that provides long-term protection in wrought Co/Ni-based superalloys.

\*\*Reywords:\*\* Superalloys, Oxidation, STEM-EDX, APT\*\*

1. Introduction

Superalloys are used in high-temperature components where both mechanical strength and oxidation resistance are essential for operation, namely the hottest sections of jet engines, such as the turbine [1]. At these high temperatures environmental degradation, such as oxidation and oxidation oxidation and oxidation oxidation and oxidation oxidation and oxidation perature, exposure time, and composition: around 5 at.% to 8 at.% Al and about 10 at.% Cr has been shown to promote protective behavior, while Ti has been shown to accelerate NiO formation and reduce scale adhesion [8-10]. Small additions of refractory elements such as Ta or

dation behavior depending on local chemistry, while Cr is vital to stable scale formation [13, 20, 22].

Understanding these regimes requires correlating oxidation kinetics with nanoscale structure and chemistry. The present study investigates oxidation in a wrought Co/Nibased superalloy exposed in air at 800 °C for 20 h, 100 h and 1000 h to represent the early, transitional, and steadystate regimes described above. Mass-gain and white-light

Table 1: Nominal	composition	in wt.%	of alloy	chosen fo	r the ex	periments	[23].

Element	Ni	Co	$\mathbf{Cr}$	$\mathbf{W}$	$\mathbf{Mo}$	Al	Ta	Nb	$\mathbf{Ti}$	$\mathbf{C}$	В	$\mathbf{Zr}$
wt.%	50.8	19.8	10.5	6.2	2.8	4.4	3.8	0.8	0.8	0.015	0.009	0.03

interferometry (WLI) help establish oxidation kinetics and surface evolution; high-resolution scanning transmission electron microscopy coupled with energy-dispersive X-ray spectroscopy (STEM-EDX) characterise the scale morphology and stratification; and atom probe tomography (APT) at 20 h helps resolve the atomic-scale chemistry of the transient scale. X-ray diffraction (XRD) investigates the phase evolution from (Ni,Co)-spinel to a mixture of chromia and alumina. These complementary techniques link the typical oxidation regimes to both structural and chemical observations, demonstrating how a transient, porous spinel evolves into a dense, adherent  ${\rm Cr_2O_3/\alpha\text{-}Al_2O_3}$  composite scale that provides long-term oxidation resistance at 800 °C [24–27].

# 2. Experimental Description

### 2.1. Oxidation Experiment

The investigated alloy was a wrought Co/Ni-based superalloy that was developed from the earlier V208 series by Knop et al. [19, 23]. Its nominal composition is given in **Table 1**. Rectangular specimens measuring 15 mm  $\times$  15 mm were mechanically polished to an in-service surface finish following standard metallographic procedures. Oxidation tests were performed in a laboratory furnace at 800 °C, with the temperature confirmed with a thermocouple. Tests were performed over three time-scales: 20 h, 100 h and 1000 h to capture early, transitional, and steady-state oxidation regimes.

Mass-gain measurements were taken using a Mettler Toledo DSC/TGA 2 instrument under static dry air to validate kinetic behavior. The mass gain per unit area and its square were plotted as functions of time to gain insight into oxidation rate laws and deviations from parabolic growth.

#### 2.2. Characterisation

XRD was performed using a Bragg–Brentano diffractometer equipped with a Cu K $\alpha$  radiation source ( $\lambda = 1.5418\,\text{Å}$ ). Scans were collected over a  $2\theta$  range of  $20^\circ$  to  $80^\circ$  with a step size of  $0.02^\circ$  and a counting time of 1 s per step. The instrument was operated at  $30\,\text{kV}$  and  $10\,\text{mA}$ , where the peaks were matched against the ICDD PDF-5+database. Surface topography was characterized by WLI to determine the average surface roughness,  $S_a$ , extracted from the reconstructed surface profiles.

Site-specific lamellae for STEM and APT were extracted using a standard in situ lift-out procedure using a Thermo Fisher Helios CX dual-beam focused ion beam—scanning electron microscope (FIB-SEM). Final polishing was performed at  $5\,\mathrm{kV}$  and  $2\,\mathrm{kV}$  to minimize surface damage and gallium implantation. All STEM datasets were acquired

using a probe-corrected Thermo Fisher Spectra 300 microscope operating at  $300\,\mathrm{kV}$ , equipped with a Bruker Dual-X energy dispersive X-ray (EDX) detector. The convergence semi-angle was approximately  $30\,\mathrm{mrad}$ . The probe current used was  $1\,\mathrm{nA}$ .

APT analysis was performed under conditions of  $50\,\mathrm{kV}$  and  $50\,\mathrm{pJ}$  using a CAMECA LEAP  $5000\mathrm{XR}$  with a pulse frequency of  $250\,\mathrm{kHz}$  and a detection rate of  $1\,\%$ . The shank angle of each specimen was taken from SEM images prior to analysis and applied for three-dimensional reconstruction. This allowed increased confidence in the correlation between atomic-scale chemistry and microstructural features observed by STEM-EDX.

Together, these complementary techniques—mass-gain, TGA, XRD, WLI, STEM-EDX, and APT—provided a multiscale dataset linking oxidation kinetics, surface evolution, and nanoscale chemistry across the three oxidation time intervals.

#### 3. Results

#### 3.1. General Oxidation Behavior

**Figure 1** shows the specific mass gain as a function of time for specimens oxidized in air at 800 °C up to 100 h. It can be seen that up to 20 h the alloy exhibits an expected near-linear increase, while by 100 h it approaches near linearity, consistent with diffusion-limited growth.

Surface topography measured by WLI and SEM are highlighted in **Figures 2–3**. At 20 h and 100 h there is a clear roughness on the surface of the grains and an apparent depression at the grain boundaries, consistent with a developing scale rich in spinel oxides; by 1000 h the surface has smoothed out highlighting the removal of these spinel oxides via spallation. Grain boundaries also seem

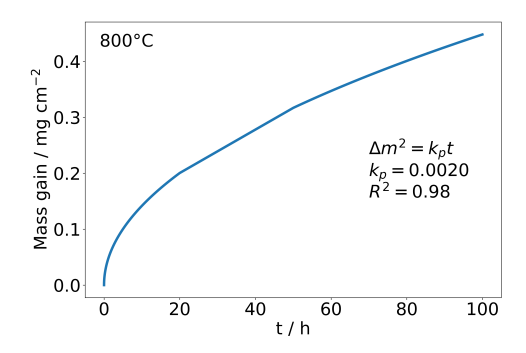


Figure 1: Mass gain versus oxidation time highlighting the isothermal oxidation behavior of the investigated alloy in static, dry air at  $800\,^{\circ}\mathrm{C}$  for the first  $100\,\mathrm{h}$  of exposure.

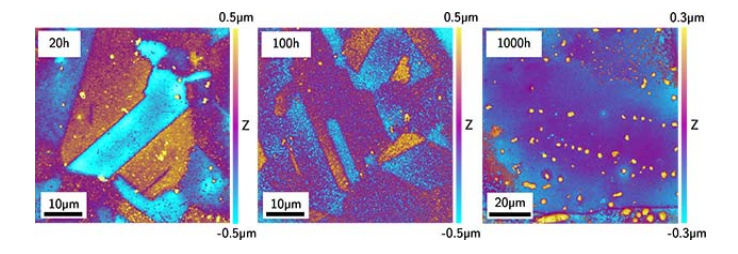


Figure 2: White light interferometry images of the chosen alloy investigated in isothermal oxidation at 800  $^{\circ}$ C for 20 h, 100 h and 1000 h.

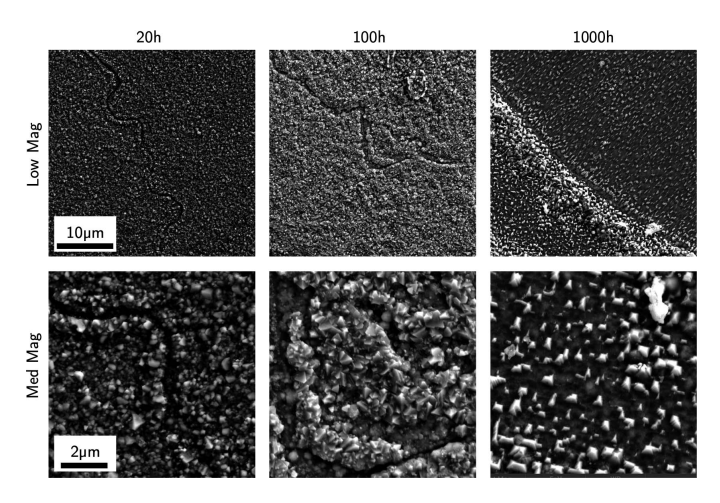


Figure 3: Secondary electron images highlighting surface roughness of the oxidised surfaces at 800 °C after 20 h, 100 h and 1000 h.

to exhibit a limited depression which suggests oxide overgrowth, enhancing protection. WLI maps help quantify these observations, shown in **Figure 3**. After 20 h the average surface roughness  $(S_a)$  was  $S_a = 0.158 \,\mu\text{m}$  with a clear depression at the grain boundary. Interestingly, depression associated with twin behavior is also observed indicating a twin-related oxidation mechanism. Similar behavior is observed after 100 h, with  $S_a = 0.105 \,\mu\text{m}$  and the same grain-boundary depressions indicating slower local oxidation in these regions. After 1000 h the overall surface is noticeably smoother with  $S_a = 0.076 \,\mu\text{m}$ . However, isolated bulging features are present near the grain boundaries. Across the series there is an apparent reduction in visible grain boundary depression, suggesting progressive overgrowth and potential grain-boundary grooving and/or infilling by the maturing oxide scale, protecting these regions.

### 3.2. Cross-Sectional Morphology and Phase Constitution

High angular dark field (HAADF) images of the oxide cross-sections are shown in **Figure 4**. At 20 h a multilayered, rough, porous oxide scale is observed with a thickness of  $1\,\mu\mathrm{m}$ . A discontinuous layer of acicular intrusions can be seen, disconnected from the bulk oxide. By  $100\,\mathrm{h}$ , a less rough, more compact scale is evident with a thickness of  $0.5\,\mu\mathrm{m}$ , and some preferential growth is also observed down the grain boundary. At  $1000\,\mathrm{h}$ , a much more densely compact multilayer is observed with smoother morphology

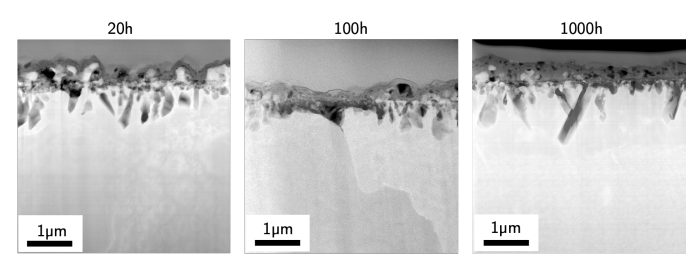


Figure 4: HAADF images taken at each time interval, highlighting scale development.

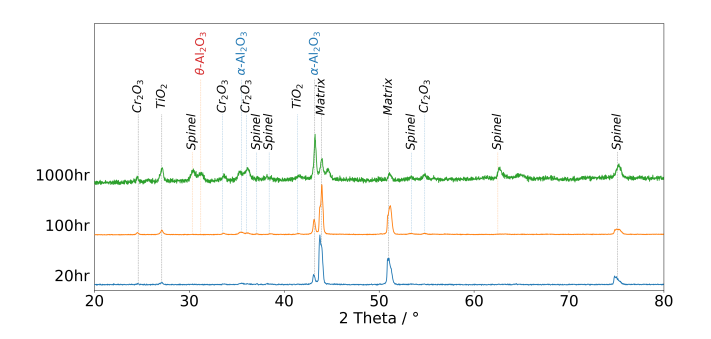


Figure 5: XRD graph highlighting the time-dependent phase development of the investigated alloy under isothermal oxidation at  $800\,^{\circ}\mathrm{C}$ 

and reduced porosity. The compact oxide layer extends to about  $0.5\,\mu\text{m}$ . The acicular layer appears more well connected; however, internal precipitates can be observed and the overall oxide damage layer depth is observed to be  $3.4\,\mu\text{m}$ .

XRD patterns for the three exposure times are shown in Figure 5. After 20 h, the diffractogram is dominated by the substrate  $(\gamma/\gamma')$  reflections, with weak contributions from spinel, Al<sub>2</sub>O<sub>3</sub> and Cr<sub>2</sub>O<sub>3</sub>, consistent with the onset of a transient outer scale. By 100 h, peaks from (Ni,Co)Cr<sub>2</sub>O<sub>4</sub> spinel and Cr<sub>2</sub>O<sub>3</sub> intensify, confirming the development of a duplex oxide with a continuous chromia layer. At 1000 h, spinel reflections are markedly reduced, while Cr<sub>2</sub>O<sub>3</sub> remains prominent and new peaks corresponding to  $\alpha$ -Al<sub>2</sub>O<sub>3</sub> appear, indicating the establishment of a dense, protective chromia-alumina bi-layer. Weak rutile (TiO<sub>2</sub>) reflections are also present at intermediate and long exposures. The apparent reduction in overall peak intensities at 1000 h suggests increased X-ray absorption and/or preferred orientation within the compact  $\alpha$ -Al<sub>2</sub>O<sub>3</sub> + Cr<sub>2</sub>O<sub>3</sub> scale, potentially compounded by peak broadening from fine  $\alpha$ -Al<sub>2</sub>O<sub>3</sub> grains. Overall, oxidation at 800 °C evolves from a transient spinel-rich scale to a chromia-dominated structure capped by  $\alpha$ -Al<sub>2</sub>O<sub>3</sub>, with alumina increasingly contributing to long-term protection.

# 3.3. Nanoscale Characterization

High-resolution STEM-EDX maps of the oxide scale after 20 h and 1000 h exposures are shown in **Figures 6–7**. At 20 h, the oxide is irregular and rough, with the outer-

most regions dominated by Co- and Ni-rich phases, corresponding to typical spinel oxides. Beneath this, a continuous Cr-rich layer is already established. For both Cr and Ni a compositional gradient is observed in the bulk metal, in which Cr becomes depleted toward the metal/oxide interface while Ni shows a slight enrichment in the same region. Bands enriched in Ti and Ta are evident, corresponding respectively to rutile (TiO<sub>2</sub>) and Ta<sub>2</sub>O<sub>5</sub>, accompanied by detectable Nb, Mo, and W signals. Numerous bubble-like features enriched in Ni, Co, and refractory elements are distributed throughout the oxide scale. Below these layers, an emerging Al-enriched layer consistent with (Al<sub>2</sub>O<sub>3</sub>) can be observed, extending as acicular intrusions into the bulk. The underlying  $\gamma'$  microstructure remains intact and closely resembles that of the heat-treated condition of the alloy prior to oxidation.

After 1000 h, the oxide has developed into a denser and more uniform structure. The layers associated with Nb, W, and Mo are no longer prominent, and most of the Ta<sub>2</sub>O<sub>5</sub> layer observed at 20 h has diminished. The outer spinel layer has become more continuous and compact, forming a more stable surface layer. A thick and persistent Cr<sub>2</sub>O<sub>3</sub> layer dominates the scale, beneath which a uniform continuous alumina layer is present. Several of the bubble-like features observed in the 20 h sample appear to have sealed within the oxide scale, still containing evidence of refractory enrichment. Ti remains locally detectable, particularly near internal precipitates within the oxide co-located with Nb in addition to the evident rutile (TiO<sub>2</sub>) layer in the scale. In the underlying alloy, the  $\gamma'$ distribution has evolved towards unimodal, with a clearly defined depletion region below the oxide scale in addition to the internal Ti/Nb-rich precipitates extending into the matrix.

APT was performed on site-specific needles extracted from the 20 h specimen, positioned within the chromia layer and extending through one of the bubble-like features into the underlying alumina region to capture the early development of these internal oxides, Figure 8. The reconstruction reveals five distinct compositional regions across the oxide scale. At the surface, a CrO<sup>+</sup>-rich zone corresponds to the chromia layer observed in STEM-EDX, showing a uniform chromium distribution with little evidence of other cations. Directly beneath, a narrow layer dominated by TaO<sup>+</sup> and TaO<sub>2</sub><sup>+</sup> ions is detected, marking a discrete Ta<sub>2</sub>O<sub>5</sub> band separating the chromia from the lower oxide regions. Beneath this, a clearly defined Al- and Oenriched region is present, consistent with alumina, within which elemental Cr<sup>+</sup> ions are also detected, suggesting local incorporation of metallic Cr. Next to the alumina, a spinel and refractory-rich zone is observed that coincides with the bubble region; this area contains elevated concentrations of Ni, Co, Ta<sup>+</sup>, Nb<sup>+</sup>, MoO<sup>+</sup>, and W, indicating the accumulation of multiple cations and complex oxide species. At the boundary between the  $(Al_2O_3)$  and the bubble, a sharp interface is noted by segregation of NbO<sup>+</sup> and WO<sup>+</sup> species, defining a clear interfacial region enriched in refractory oxides.

#### 4. Discussion

The oxidation behavior of this wrought Co/Ni-based superalloy at 800 °C shows a clear time-dependent evolution linking surface morphology, phase constitution, and nanoscale chemistry. The transition from initial rapid oxidation to slower, diffusion-controlled growth is reflected in both the curvature of the mass-gain curves and the surface roughness reduction across the time scales. The nearlinear kinetics at 20 h correspond to cation-driven growth through a rough, spinel-rich surface layer, consistent with early-stage oxidation reported in Co- and Ni-base systems where outward cation diffusion dominates before a continuous chromia barrier forms [28, 29]. The subsequent reduction in rate coincides with the development and thickening of a dense Cr<sub>2</sub>O<sub>3</sub> layer, which acts as an effective diffusion barrier. This progressive increase in stability shown by the WLI observations, showing a smoother overall surface at 1000 h with limited bulging of Cr-rich oxide and reduced roughness relative to earlier exposures.

At short timescales, the alloy surface oxidizes rapidly to form a rough scale dominated by (Ni,Co)(Cr,Al)<sub>2</sub>O<sub>4</sub> spinel and a chromia band that has already been established. Ni-rich regions are seen throughout the surface of the scale, which displays depressions along grain boundaries, highlighting preferential oxidation down the grain boundaries which act as fast-diffusion pathways. Oxygen penetration down the boundaries promotes inward growth of oxide, producing the characteristic trough-like features captured by WLI. Beneath the spinel layer, a continuous Cr-rich layer with a thin alumina enriched zone beneath it can be seen, marking the onset of sub-scale alumina formation. Discrete Ti- and Ta-containing bands are also visible within this region, corresponding to rutile-TiO<sub>2</sub> and Ta<sub>2</sub>O<sub>5</sub>, which have been observed in Ti- and Ta-bearing superalloys exposed at similar temperatures and shown to be detrimental [28]. Nb, W, and Mo are detected at lower concentrations throughout the scale, however, the APT analysis highlights the complex transition through the oxide layer. The uppermost region is dominated by CrO<sup>+</sup> ions, consistent with the chromia layer detected by STEM-EDX. Immediately beneath this, a narrow zone rich in TaO<sup>+</sup> and TaO<sub>2</sub><sup>+</sup> species is observed. These ions represent field-evaporation fragments of Ta<sub>2</sub>O<sub>5</sub>, as the molecular Ta<sub>2</sub>O<sub>5</sub><sup>+</sup> species are too heavy to remain stable under APT analysis conditions. This confirms the presence of a thin tantalum-oxide band separating the chromia, alumina and spinel regions.

Below this zone, a mixed Ni, Co, and refractory-rich region corresponds to the internal oxide bubble observed in STEM-EDX. At the interface between this region and the alumina, pronounced segregation of NbO<sup>+</sup> and WO<sup>+</sup> species defines a sharp interfacial boundary enriched in refractory oxides. Similar Nb- and W-oxide segregation to chromia/alumina interfaces has been reported in Ni-

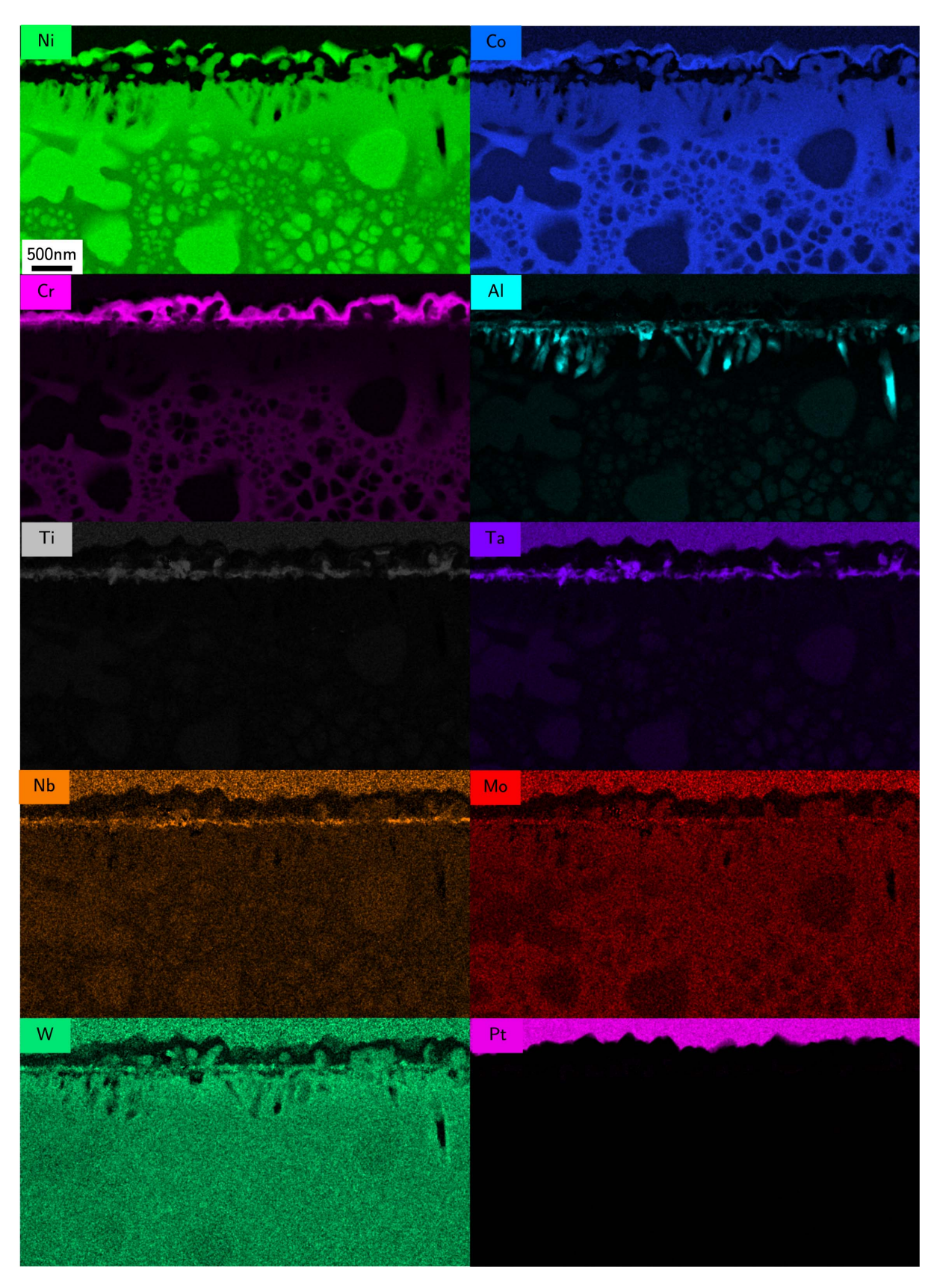


Figure 6: STEM-EDX of the cross-section of the investigated alloy after isothermal oxidation at  $800\,^{\circ}\mathrm{C}$  for  $20\,\mathrm{h}$ . Maps shown in at %.

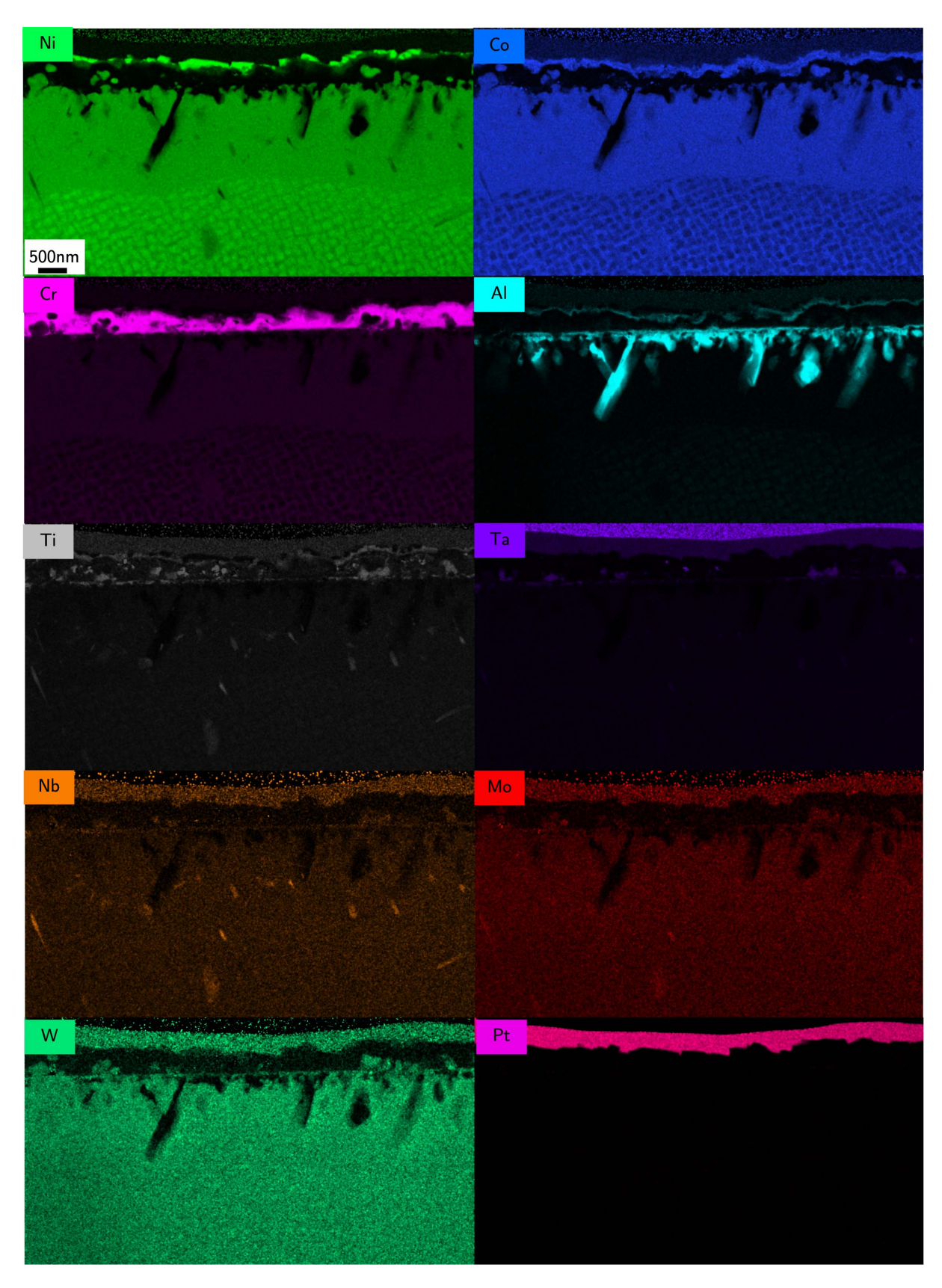


Figure 7: STEM-EDX of the cross-section of the investigated alloy after isothermal oxidation at  $800\,^{\circ}\mathrm{C}$  for  $1000\,\mathrm{h}$ . Maps shown in at.%.

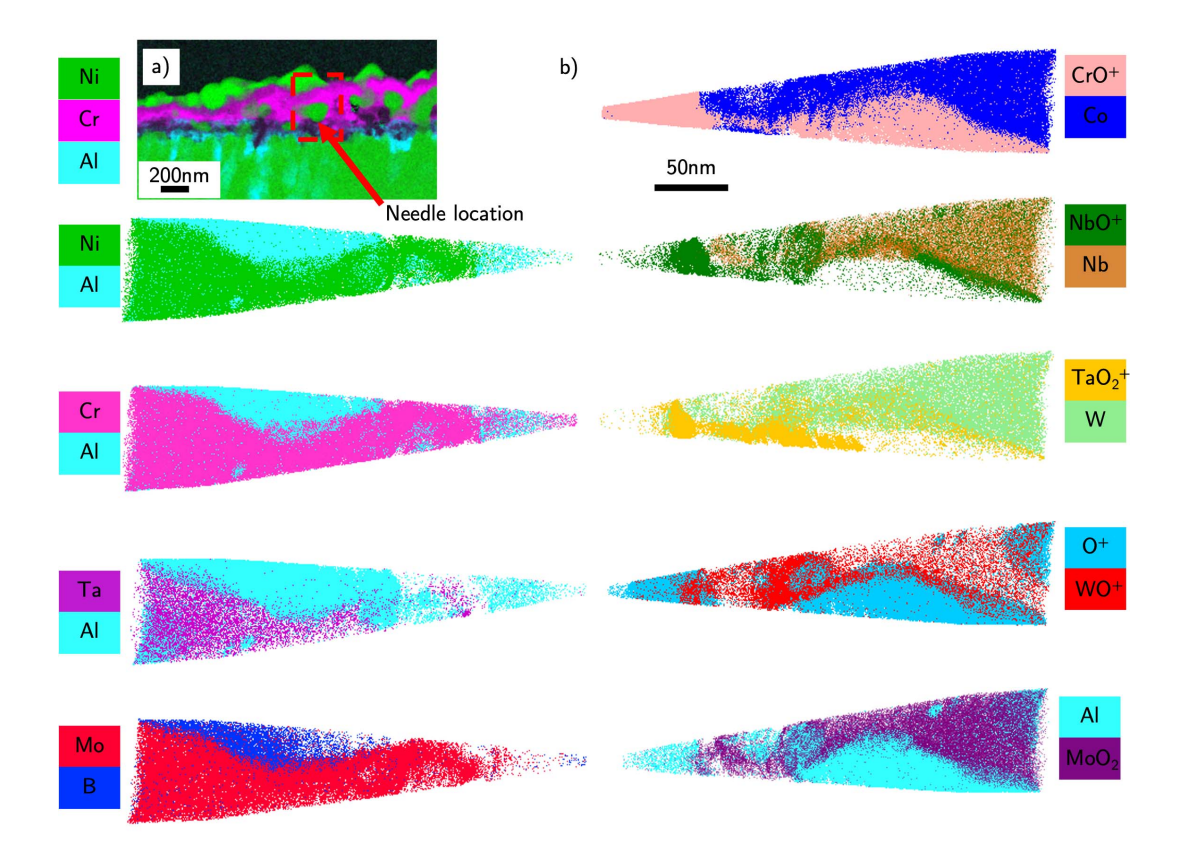


Figure 8: (a) STEM-EDX image of the APT needle lift-out location through  $Cr_2O_3$  scale and refractory-rich spinel bubble into the  $Al_2O_3$  fingers on 20 h oxidized sample. (b) APT needle reconstructions obtained for different species.

and Co-base alloys and attributed to the low mobility and high oxygen affinity of these elements under intermediate oxygen potentials [13, 30]. These likely form where the oxygen potential is lowest, causing Nb and W to oxidize partially and accumulate at the migrating alumina—spinel interface. Such refractory enrichment suggests potential kinetic trapping of slow-diffusing cations at the internal boundary.

Beneath this lies an Al- and O-enriched region consistent with the acicular alumina layer, within which elemental Cr<sup>+</sup> ions are also detected. The incorporation of chromium within the alumina likely arises from upward diffusion of Cr through the sub-scale oxide during its migration toward the chromia layer. Interestingly, boron is seen to segregate within the aluminum rich region. It is hypothesized here that boron could potentially play a role in stabilizing the alumina scale and increasing scale adherence.

As oxidation progresses to  $100\,h$ , the XRD results indicate the development of a more stratified oxide structure. The increased intensity of spinel and  $\rm Cr_2O_3$  peaks suggests the formation of a duplex scale consisting of an outer (Ni,Co)-spinel region and an inner chromia-rich band. The emergence of a continuous chromia component likely marks a turning point in the oxidation process, as chromia generally exhibits lower oxygen-ion conductivity and a finer-grained morphology than spinel, both of which restrict

mass transport. This transition toward chromia control coincides with the observed reduction in apparent oxidation rate and likely precedes the eventual establishment of a continuous alumina sub-layer at longer durations. Internal oxidation penetrating down grain boundaries is also observed, consistent with oxygen ingress through high-diffusivity boundary paths.

After 1000 h exposure, the scale appears to reach a more stable configuration characterized by a dense, adherent oxide scale composed of  $\rm Cr_2O_3$ , with a more continuous  $\alpha$ -Al<sub>2</sub>O<sub>3</sub> sub-layer developed beneath it. The chromia layer remains compact and continuous. Meanwhile, the refractory-rich oxides (W, Nb, Ta) observed at earlier stages are only seen as isolated regions trapped between chromia and alumina, suggesting they are most likely residues rather than active diffusion barriers.

The WLI shows reduced surface roughness, and the depressions previously observed at grain boundaries have largely disappeared, indicating local overgrowth and the establishment of uniform scale coverage across grains.  $\alpha$ -Al<sub>2</sub>O<sub>3</sub> reflections in XRD appear to get stronger and the weakening of the spinel peaks confirm progressive transformation of the scale towards a dual chromia—alumina scale structure. The  $\theta \to \alpha$  transition of alumina involves significant volume shrinkage and defect annihilation, reducing both oxygen permeability and cation vacancy concentration [31]. The resulting scale suppresses mass oxygen

transport, most likely accounting for the observed longterm parabolic oxidation behavior.

A further notable feature is the apparent crystallographic dependence of oxidation, particularly the behaviour of the present annealing twins. WLI results revealed that regions corresponding to coherent twin bands exhibit significantly reduced oxide growth compared to the surrounding matrix, consistent with the lower surface reactivity and diffusivity expected for  $\Sigma 3$  boundaries. Similar effects have been reported in Ni- and Co-based superalloys and other alloy systems, where twins act as barriers to oxide nucleation or slow lateral scale growth due to their low-energy character and limited dislocation content [32, 33]. The reduced oxidation along these coherent interfaces may therefore contribute to the smoother long-term surface morphology observed after extended exposure, as neighboring grains overgrow and homogenize the scale topography.

The progressive surface smoothing observed by WLI  $(S_a \text{ decreasing from } 0.158 \,\mu\text{m to } 0.076 \,\mu\text{m})$  is directly linked to the phases and chemistry of the oxide scale. The initially rough, spinel-rich surface at 20 h (Figure 2) represents a kinetically favored transient state. Subsequently, thermodynamically stable  $Cr_2O_3$  and  $\alpha$ -Al<sub>2</sub>O<sub>3</sub> layers form beneath it, as confirmed by STEM-EDX. This new, adherent sub-scale undermines the original, poorly adherent spinel. Spinel spallation is therefore the most probable primary cause of the smoother surface highlighted by the reduced spinel reflections in the 1000 h XRD data. The 1000 h morphology thus represents this compact, stable  $Cr_2O_3/\alpha$ -Al<sub>2</sub>O<sub>3</sub> layer rather than a relaxation of the original one. The reduction in visible grain-boundary depression further supports this, suggesting progressive overgrowth by the chromia, which blocks fast diffusion paths and lowers the overall oxidation rate down the grain boundaries.

The oxidation process appears to involve three overlapping regimes. Initially, dominant outward cation diffusion produces a porous spinel scale and high mass gain. Subsequently, mixed diffusion (inward oxygen and lateral chromia growth) establishes a semi-protective, multilayered structure. Finally, a continuous  $\alpha$ -Al<sub>2</sub>O<sub>3</sub> layer forms, restricting both oxygen and cation transport and yielding a parabolic rate law with improved adhesion. The alloy's chemistry promotes early alumina nucleation without the volatility issues typical of Co-rich oxides, while Cr acts synergistically by forming a temporary chromia barrier that accelerates the densification of the scale. Refractory-rich "bubbles" retained at the chromia—alumina interface likely represent trapped remnants of transient oxides, marking the transition from mixed to protective scale growth.

The integrated kinetic, structural, and chemical evidence demonstrates that oxidation of this wrought Co/Ni alloy proceeds through a classical transformation sequence typical of a type II alloy: Ni/Co-spinel  $\rightarrow$  external Cr<sub>2</sub>O<sub>3</sub> + internal  $\alpha$ -Al<sub>2</sub>O<sub>3</sub>, culminating in a dense, continuous chromia + alumina scale. The combined use of WLI, SEM, XRD, STEM-EDX, and APT provides a complete multi-

scale view of this evolution—from bulk kinetics to atomic-scale segregation—revealing how a transient, porous oxide converts into a self-protecting barrier capable of sustaining long-term stability at 800 °C.

### 5. Conclusion

The oxidation behavior and mechanisms of a novel wrought Co/Ni-based superalloy were characterized through complementary mass-gain kinetics, XRD, SEM/WLI, and STEM-EDX analyses, supported by local nanoscale chemical insights from APT at early stages. Isothermal oxidation tests were conducted at 800 °C for 20 h, 100 h and 1000 h to capture the transition from transient to steady-state oxidation. The following conclusions can be drawn:

- The alloy exhibits a clear transition from rapid, nearlinear oxidation at 20 h to parabolic, diffusion-controlled behavior by 100 h and beyond. The reduction in the apparent rate constant reflects the development of a more stable scale and a shift from outward cation to inward oxygen transport control.
- 2. Surface characterisation by WLI and SEM revealed a systematic smoothing of the oxide with exposure time: from ridge-like spinel growth at 20 h ( $S_a \approx 1.6 \,\mu\text{m}$ ), to partial coalescence and shallow spallation at 100 h ( $S_a \approx 1.1 \,\mu\text{m}$ ), and finally to a compact, adherent surface at 1000 h ( $S_a \approx 0.7 \,\mu\text{m}$ ). The disappearance of boundary depressions indicates overgrowth and protection of grain boundaries, while WLI also shows that coherent twin bands oxidize more slowly than the surrounding matrix, consistent with the low reactivity and diffusivity associated with  $\Sigma 3$  interfaces. Together, these effects produce a uniform and mechanically stable surface at long exposures.
- 3. XRD analysis showed a sequential phase transformation from an outer (Ni,Co)(Cr,Al)<sub>2</sub>O<sub>4</sub> spinel and NiO at 20 h, through a duplex chromia–spinel structure at 100 h, to a dense Cr<sub>2</sub>O<sub>3</sub> layer with a continuous  $\alpha$ -Al<sub>2</sub>O<sub>3</sub> sub-layer at 1000 h. This progressive structural refinement accounts for the observed kinetic slowdown and long-term stability of the oxide.
- 4. Combined STEM-EDX and APT analyses revealed that Al and Cr selectively oxidize from the earliest stages, forming an incipient Al–O-rich transition zone that subsequently develops into a continuous alumina band beneath the chromia. APT further resolved chemical behavior within the complex scale, including CrO<sup>+</sup>-rich zones corresponding to chromia, a narrow TaO<sup>+</sup>/TaO<sub>2</sub><sup>+</sup> band indicative of Ta<sub>2</sub>O<sub>5</sub>, and NbO<sup>+</sup>/WO<sup>+</sup> segregation defining a refractory-enriched interfacial boundary. These findings suggest that Ti- and Ta-rich oxides (rutile and Ta<sub>2</sub>O<sub>5</sub>) form transiently, while Nb- and W-rich oxides persist as isolated inclusions trapped between chromia and

- alumina after prolonged exposure. The refractoryrich "bubbles" thus most likely represent inert residues of the early transient regime and mark the transition from mixed to protective scale growth.
- 5. Overall, oxidation at 800 °C follows a typical Type II sequence of Ni/Co-spinel  $\rightarrow$  Cr<sub>2</sub>O<sub>3</sub>  $\rightarrow$   $\alpha$ -Al<sub>2</sub>O<sub>3</sub>. The balanced chemistry enables early alumina formation while Cr provides a transient chromia barrier that accelerates scale stability. The resulting dual chromia–alumina structure allows for improved oxidation resistance.

# Acknowledgements

The authors would like to acknowledge support from Rolls-Royce plc for their continued support and funding. MC acknowledges funding from Royal Society Tata University Research Fellowship URF/R1/201318, Royal Society Enhancement Award RF/ERE/210200EM1, and ERC CoG DISCO grant 101171966.

## References

- [1] R. Reed, The superalloys: fundamentals and applications, Cambridge University Press, 2006.
- [2] S. Bose, High Temperature Coatings, 2nd Edition, Butterworth-Heinemann, Langford, Australia, 2017.
- [3] L. Klein, M. Killian, S. Virtanen, The effect of nickel and silicon addition on some oxidation properties of novel Co-based high temperature alloys, Corrosion Science 69 (2013) 43–49. doi:10.1016/j.corsci.2012.09.046.
- [4] C. S. Giggins, F. S. Pettit, Oxidation of Ni-Cr-Al Alloys Between 1000° and 1200°C, Journal of The Electrochemical Society 118 (11) (1971) 1782. doi:10.1149/1.2407837.
- [5] C. Wagner, Theoretical Analysis of the Diffusion Processes Determining the Oxidation Rate of Alloys, Journal of The Electrochemical Society 99 (10) (1952) 369. doi:10.1149/1.2779605.
- [6] R. Prescott, M. J. Graham, The formation of aluminum oxide scales on high-temperature alloys, Oxidation of Metals 38 (3-4) (1992) 233–254. doi:10.1007/BF00666913.
- [7] Z. Liang, M. Göken, U. Lorenz, S. Neumeier, M. Oehring, F. Pyczak, A. Stark, L. Wang, Influence of small amounts of Si and Cr on the high temperature oxidation behavior of novel cobalt base superalloys, Corrosion Science 184 (2021) 109388. doi:10.1016/j.corsci.2021.109388.
- [8] S. Ma, Q. Ding, X. Wei, Z. Zhang, H. Bei, The Effects of Alloying Elements Cr, Al, and Si on Oxidation Behaviors of Ni-Based Superalloys, Materials 15 (20) (2022) 7352. doi:10.3390/ma15207352.

- [9] S. Park, S. Seo, Y. Yoo, H. Jeong, H. Jang, Effects of Al and Ta on the high temperature oxidation of Nibased superalloys, Corrosion Science 90 (2015) 305– 312. doi:10.1016/j.corsci.2014.10.025.
- [10] S. Yang, Effect of Ti and Ta on the oxidation of a complex superalloy, Oxidation of Metals 15 (5-6) (1981) 375–397. doi:10.1007/BF00603531.
- [11] M. Donachie, Superalloys: A Technical Guide, ASM International, Materials Park, OH, 2002.
- [12] L. Klein, A. Bauer, S. Neumeier, M. Göken, S. Virtanen, High temperature oxidation of  $\gamma/\gamma'$ -strengthened Co-base superalloys, Corrosion Science 53 (5) (2011) 2027–2034. doi:10.1016/j.corsci.2011.02.033.
- [13] X. Ye, B. Yang, Y. Nie, S. Yu, Y. Li, Influence of Nb addition on the oxidation behavior of novel Nibase superalloy, Corrosion Science 185 (2021) 109436. doi:10.1016/j.corsci.2021.109436.
- [14] C. A. Barrett, R. V. Miner, D. R. Hull, The effects of Cr, Al, Ti, Mo, W, Ta, and Cb on the cyclic oxidation behavior of cast Ni-base superalloys at 1100 and 1150 °C, Oxidation of Metals 20 (5-6) (1983) 255–278. doi:10.1007/BF00656844.
- [15] H. Yan, V. Vorontsov, J. Coakley, N. Jones, H. Stone, D. Dye, Quaternary Alloying Effects and the Prospects for a New Generation of Co-Base Superalloys, in: Superalloys 2012, Wiley, 2012, pp. 705–714. doi:10.1002/9781118516430.ch78.
- [16] J. Sato, T. Omori, K. Oikawa, I. Ohnuma, R. Kainuma, K. Ishida, Cobalt-base hightemperature alloys, Science 312 (5770) (2006) 90-91. doi:10.1126/science.1121738.
- [17] Y. Zhang, H. Fu, F. Zhou, J. Xie, Revealing the effect of Al content on the oxidation of  $\gamma'$ -strengthened cobalt-based superalloys, Corrosion Science 198 (2022) 110122. doi:10.1016/j.corsci.2022.110122.
- [18] L. Li, L. Wang, Z. Liang, J. He, J. Qiu, F. Pyczak, M. Song, Effects of Ni and Cr on the high-temperature oxidation behavior and mechanisms of Co- and CoNibase superalloys, Materials & Design 224 (2022) 111291. doi:10.1016/j.matdes.2022.111291.
- [19] M. Knop, P. Mulvey, F. Ismail, A. Radecka, K. M. Rahman, T. C. Lindley, B. A. Shollock, M. C. Hardy, M. P. Moody, T. L. Martin, P. A. Bagot, D. Dye, A New Polycrystalline Co-Ni Superalloy, JOM 66 (12) (2014) 2495–2501. doi:10.1007/s11837-014-1175-9.
- [20] H. Yan, V. Vorontsov, D. Dye, Alloying effects in polycrystalline  $\gamma'$  strengthened Co–Al–W base alloys, Intermetallics 48 (2014) 44–53. doi:10.1016/j.intermet.2013.10.022.

- [21] B. Gao, L. Wang, Y. Liu, X. Song, S. Yang, A. Chiba, High temperature oxidation behaviour of  $\gamma'$ -strengthened Co-based superalloys with different Ni addition, Corrosion Science 157 (2019) 109–115. doi:10.1016/j.corsci.2019.05.036.
- [22] Y. Zhang, Z. Li, Y. Gui, H. Fu, J. Xie, Effect of Ti and Ta content on the oxidation resistance of Co-Ni-based superalloys, International Journal of Minerals, Metallurgy and Materials 31 (2) (2024) 351–361. doi:10.1007/s12613-023-2733-3.
- [23] M. Hardy, D. Dye, L. Reynolds, T. McAuliffe, I. Bantounas, EP003957761A1 (71) Applicant: Rolls-Royce plc London N1 9FX (GB) (2 2022). doi:10.08.2021.
- [24] C. Liu, J. Ma, X. Sun, Oxidation behavior of a single-crystal Ni-base superalloy between 900 and 1000°C in air, Journal of Alloys and Compounds 491 (1-2) (2010) 522–526. doi:10.1016/j.jallcom.2009.10.261.
- [25] C. Rodenkirchen, M. Appleton, M. P. Ryan, S. Pedrazzini, A review on atom probe and correlative microscopy studies of corrosion in nickel-based superalloys, MRS Bulletin 47 (7) (2022) 706–717. doi:10.1557/s43577-022-00366-7.
- [26] J. W. X. Wo, M. C. Hardy, H. J. Stone, The Effect of Nb, Ta, and Ti on the Oxidation of a New Polycrystalline Ni-Based Superalloy, High Temperature Corrosion of Materials 101 (3) (2024) 485–509. doi:10.1007/s11085-023-10218-7.
- [27] D. Blavette, E. Cadel, B. Deconihout, The Role of the Atom Probe in the Study of Nickel-Based Superalloys, Materials Characterization 44 (1-2) (2000) 133–157. doi:10.1016/S1044-5803(99)00050-9.
- [28] G. Wang, J. Zhang, Y. Li, D. Zhao, Y. Yang, Q. Li, K. Xie, The synergy effect of elements on the oxidation resistance of a high-purity directionally solidification nickel-based superalloy, Journal of Materials Research and Technology 26 (2023) 2796–2805. doi:10.1016/j.jmrt.2023.08.054.
- [29] H. Tian, J. Zhang, Y. Wu, J. Chen, Co-evolution Mechanism of Oxidation Kinetics and Precipitates of IC10 Nickel-Based Superalloy Under Temperature Gradient and Its Effect on Mechanical Properties, Metallurgical and Materials Transactions B 56 (5) (2025) 4524–4534. doi:10.1007/s11663-025-03718-1.
- [30] F. Weng, H. Yu, C. Chen, K. Wan, Influence of Nb and Y on Hot Corrosion Behavior of Ni–Cr-based Superalloys, Materials and Manufacturing Processes 30 (5) (2015) 677–684. doi:10.1080/10426914.2014.994770.
- [31] Y. Huang, X. Peng, X. Chen, The mechanism of  $\theta$  to  $\alpha$ -Al2O3 phase transformation, Journal of Alloys and Compounds 863 (2021) 158666. doi:10.1016/j.jallcom.2021.158666.

- [32] S. Yamaura, Y. Igarashi, S. Tsurekawa, T. Watanabe, Structure-dependent intergranular oxidation in Ni–Fe polycrystalline alloy, Acta Materialia 47 (4) (1999) 1163–1174. doi:10.1016/S1359-6454(99)00007-5.
- [33] A. Yeh, Y. Huang, T. Tsao, S. Chang, M. Li, S. Kuo, C. Kuo, Investigations on the high temperature properties of a superalloy after microstructure engineering, Journal of Alloys and Compounds 605 (2014) 142–148. doi:10.1016/j.jallcom.2014.03.170.